Retrofitting Seismically Damaged Steel sections encased Concrete Composite Walls using Externally Bonded CFRP Strips

Fang-Jin Sun[1], Shao-Hua Pang[2], Zhong-Wen Zhang[2], Feng Fu[3], and Kai Qian[1*]

[1]College of Civil Engineering and Architecture, Guilin University of Technology, Guilin, China, 541004

[2] Guangxi Hualan Design Co. LTD, Nanhua Dong Road, Nanning, China, 514500

[3] School of Mathematics, Computer Science and Engineering ,City, University of London, U.K.,

Abstract:

Concrete shear wall encased with steel sections were widely used in high rise buildings due to its high lateral strength, ductility and energy dissipation capacity. However, to date, little studies were conducted on repairment of seismically damaged steel-concrete composite (SCC) walls to recover their lateral load resisting capacity. Thus, the efficiency of Carbon Fiber Reinforced Polymers (CFRP) strips to retrofit SCC walls after earthquake was unclear. For this purpose, four SCC walls were first tested to failure under cyclic lateral loads and thereafter repaired and re-tested. The first crack load, crack pattern, yield load, and peak load of tested specimens were measured and compared. It was found that replacing buckled rebar and applying proper CFRP repairing scheme could recover the seismic resistance of damaged SCC walls . However, if purely rely on CFRP repairing schemes without replacing of the buckled rebar, the yield load, peak load, and initial stiffness could not be properly recovered. However, as long as CFRP repairing schemes applied, the degradation of strength and stiffness of repaired specimens was slower than that of counterpart without retrofitting , which resulted in enhancement of relatively larger drift ratio.

Keywords: Steel-concrete composite, Structural wall, Seismic, CFRP, Repair.

* Corresponding author. Tel.: 65+67905292, E-mail address: qiankai@ntu.edu.sg

1. Introduction

Due to superior lateral stiffness and ductility, steel-concrete composite (SCC) walls embedded with steel sections are commonly used in high-rise building in relatively high seismic activity zone [1]. There are different types of SCC walls. Wright and Gallocher [2] and Wright [3] studied the behavior of SCC walls made of steel plates infilled with concrete in the core. Emori [4], Dan et al. [5,6], and Lan et al. [7,8] carried out tests to investigate the axial load and lateral load resisting capacity of reinforced concrete (RC) walls with encased shape steel. Actually, RC structural components with encased steel sections have been investigated extensively [9-13]. In general, these investigations had revealed that RC structural components with encased steel sections performed well in terms of load resisting capacity, ductility, and deformation capacity [10]. However, when SCC walls subjected to considerable damage after seismic loads, demolition of the whole building was commonly adopted [14]. However, if seismically damaged SCC walls could be repaired, the buildings could recover its function timely which will be cost effective and benefit and the environment. Regarding strengthening and retrofitting, externally bonded fiber-reinforced polymer (FRP) strips or sheets is widely used due to their corrosion resistance, ease of application and tailorability, and high strength-to-weight ratio. Moreover, the orientation of the FRP strips could be adjusted to meet the strengthening objectives [14].

Li et al. [15], Zhang et al. [16], Popescu et al. [17-18], Lima et al. [19], Li and Lim [20] investigated the efficiency of FRP composites for strengthening and rehabilitation of RC walls. It was found that the FRP composites could recover the seismic performance in terms of lateral stiffness, deformation capacity, and energy dissipation capacity well. Shen et al. [21], Katrizadeh and Narmashiri [22], Altaee et al. [23], and Amoush and Ghanem [24] conducted experimental tests on strengthening steel or steel-concrete composite structural components using externally bonded FRP composites. However, majority of these tests focused on steel or composite girder, beam, or column.

To date, very little tests had been carried out on FRP composites repairing seismically damaged SCC walls. To deeper understand the efficiency of FRP composites for repairing seismically damaged SCC walls and to reveal the possible change of failure mode of repaired walls, a series of five SCC walls were tested subjected to repeated cyclic lateral load to failure (lateral load resisting capacity dropped over 15 %). Then, the damaged walls were repaired by two different rehabilitation schemes using externally bonded FRP strips or sheets. Finally, the repaired specimens were re-tested and compared with the control specimens. It was found that replacing buckled rebar and applying proper CFRP repairing scheme could recover the seismic resistance of damaged SCC walls . However, if purely rely on CFRP repairing schemes without replacing of the buckled rebar, the yield load, peak load, and initial stiffness could not be properly recovered. However, as long as CFRP repairing schemes applied, the degradation of strength and stiffness of repaired specimens was slower than that of counterpart without retrofitting , which resulted in enhancement of relatively larger drift ratio.

2. Experimental Program

2.1. Design of Control Specimens

Four 1/2 scaled single-curvature specimens (SW1, SW2, SW3, and SW4) were tested at Guangxi University, China to investigate seismic behavior of SCC walls with different arrangement of prestressed bracing. SW1 is an RC wall without any prestressed bracing, as shown in **Fig. 1a**. SW2 and SW3 are reinforced with X-shaped bracing running from base to top, as shown in **Fig. 1b.** Threaded tension rods with diameter of 20 mm were used as prestressed bracing. As post-tensioning technique was adopted, polyvinyl chloride (PVC) duct was embedded before casting. The tension rods were anchored to the wall by the steel plate welded with the steel cages in the wall. The difference between SW2 and SW3 were the effective prestressing force in the tension rod, as shown in **Table 1**. For SW4, similar to SW2 and SW3, X-shaped bracing was installed. However, different to SW2 and SW3, the PVC duct was replaced by rectangular steel tube with size of 40×30×3, as shown in **Fig. 1c**.

2.2. *Material Properties*

The average concrete compressive strength of control specimen is 53 MPa based on six 150 mm×150 mm ×150 mm cube test. The property of reinforcements and prestressing bracing is provided in **Table 2** while the property of CFRP strips is shown in **Table 3**.

2.3. Test Setup and Instrumentation

As shown in **Fig. 2**, single-curvature bending was designed for tested walls. The bottom of the wall (1520 mm length, 500 mm height, and 400 mm width) was fixed to the strong floor by four prestressing rods. The vertical axial force was applied by a hydraulic jack. During tests, the vertical axial force remains constant to simulate the effect of the gravity load. To eliminate the friction force, a series of pins were installed above the jack. Moreover, a steel loading frame was used to evenly distribute the axial force. The lateral load was applied at the center of the top foundation (720 mm length, 400 mm height, and 400 mm width) by a hydraulic actuator. To prevent the out-of-plane failure, a steel assembly was installed to restrain the out-of-plane movement of the wall. For specimens with post-tensioning rods or braces, the post-tensioning force was applied by hydraulic jack before testing. However, it should be noted that the post-tensioning force was not adjusted after test even it began to decrease due to concrete crushing or other reasons. As shown in **Fig. 3**, the loading program was displacement-controlled and gradually increased drift ratio (DR) with incremental of 0.25 %. For each DR, the load cycle repeated three times.

Necessary instrumentations and devices were installed externally or internally to measure the key results. The axial force applied on the wall top was measured from the reading of oil pump. The lateral displacement and force were measured by built-in load cell and displacement transducer. A series of displacement transducers were installed along the wall height to measure the shear and flexural deformation. Moreover, two displacement transducers were installed beneath the bottom foundation to monitor the rigid movement of the wall. Strain gauges were glued on reinforcements to monitor local behavior of the specimens.

2.4 Seismic Behavior and Failure Mode of Control Specimens

Fig. 4 shows the comparison of the backbone curve of the control specimens while **Table 4** listed the key results. The first crack load of SW1, SW2, SW3, and SW4 were 126.5 kN, 164.0 kN, 180.0 kN, and 160 kN, respectively. Therefore, the prestressing rod increased the first crack load by 29.6 %, 42.3 %, and 26.4 %, respectively. Moreover, the displacement at the first crack load of SW1, SW2, SW3, and SW4 were 1.18 mm, 1.38 mm, 2.19 mm, and 1.76 mm, respectively. Therefore, the prestressing rod delayed the first crack effectively. However, yield load of SW1, SW2, SW3, and SW4 were 284.3 kN, 287.8 kN, 285.9 kN, and 307.2 kN, respectively. Therefore, the prestressing rod with PVC tube (SW2 and SW3) will not increase the yield load significantly while the prestressing rod with steel tube could increase the yield load by 8.1 %. It should be noted that the first yield load was determined based on energy equilibrium method, as shown in **Fig. 5**. Furthermore, the peak load of SW1, SW2, SW3, and SW4 were 348.7 kN, 354.8 kN, 351.5 kN, and 368.5 kN, respectively. Similar to the yield load, the prestressing rod has little effects on enhancing the peak load, which could be explained by the shear cracks and deformation aggravate the loss of prestressing force. The displacement at peak load of SW1, SW2, SW3, and SW4 was 11.0 mm, 11.5 mm, 11.5 mm, and 14.8 mm. Finally, as shown in **Fig. 4**, the strength degradation was gradually for all of the specimens. The failure mode of the control specimens were shown in **Fig. 6**. As shown in the figure, all specimens have similar failure modes. The diagonal cracks became wider with the increase of lateral load. At the same time, severe spalling of concrete and rebar buckling were observed at the flange of the walls. Moreover, for SW2 and SW3, the channel steel at the flange was also fractured. However, the X-shaped prestressing rod could delay the emergence of the first crack. Moreover, the prestressing rods could reduce the number of diagonal cracks, especially for SW3. For details of the test results of the control specimens, please refer to the Lan et al. [25].

3 Rehabilitation and Repairing

As shown in **Fig. 7**, the fragment of concrete was removed first. Then, the fractured or buckled reinforcement were replaced by T10 rebar with arc welding in Specimens SW1 and SW2. The length of replaced rebar was larger than 5d. For SW3 and SW4, the buckled reinforcements were not replaced, as given in **Table 1**. It should be noted that the fracture of the channel steel was not repaired for all specimens due to difficulty in operation. After that, non-shrink but high strength mortar was used to repair the thin cracks while pea gravel concrete with strength of 45 MPa was used to replace the removed fragment of concrete. Before application of CFRP strips, the regions, which will be bonded to the CFRP laminates, were grinded to achieve a fully smooth surface. The concrete edges were rounded at a radius of about 20 mm to ensure the effectiveness of the confining solution due to CFRP laminates.

The repairing scheme was designed based on the failure mode of the control specimens. As shown in **Fig. 8a**, for Specimens RW2 and RW3, repairing scheme 1 was adopted. Firstly, two layers of diagonal strips with width of 150 mm were attached to both face of the wall to restoring the shear strength (the diagonal cracks were just injected by mortar). Secondly, two layers of C-shaped CFRP sheet were attached at both flange of the wall as the fracture of channel steel was not repaired. The layer of C-shaped CFRP sheet was determined using Eq. 1. As shown in the figure, to fully develop the strength of C-shaped CFRP sheet, the sheets were extended enough length in three directions.

$$n = \frac{A_c f_{yc}}{A_{FRP} f_{uFRP}} \tag{1}$$

where n is the layer of the C-shaped CFRP sheet, A_c is the area of the channel steel, f_{yc} is the yield strength of the channel steel, A_{FRP} is the area of single layer of the C-shaped CFRP sheet, and f_{uFRP} is the ultimate strength of CFRP sheet.

Finally, CFRP strips with width of 100 mm was wrapped the wall with spacing of 500 mm to delay the debonding of the CFRP strips or sheets. Specimen RW4 was repaired by CFRP scheme 2. Different to RW2 and RW3, the diagonal strips were replaced by vertical strips with width of 100 mm, distributed with spacing of 360 mm. Regarding the C-shaped CFRP sheets and horizontal wrapped CFRP strips, identical to that of scheme 1.

4. Comparative Study of re-testing result and Discussion

4.1. General behavior and failure mode of repaired specimens during re-testing

4.1.1 RW1

Before DR reached 0.5 %, no cracks and CFRP debonding were observed. However, at DR of 0.75 %, sound due to debonding of CFRP laminates was heard. However, no evident cracks was observed due to wrapping of CFRP laminates. Further increasing DR to 1.0 %, slight debonding was observed at the side of wall bottom, which means concrete crushing occurred there. At DR of 1.25 %, severe CFRP debonding occurred at the position where 320 mm from the top of bottom foundation. The main crack began to develop toward the bottom corner of the wall. At DR OF 1/5 %, the bulk of cracks at CFRP sheets at the corner of the wall developed quickly and tearing of CFRP sheet occurred due to severe concrete crushing. After that, the debonding of CFRP sheet becomes more obvious. At DR of 2.0 %, fully delamination of C-shaped CFRP sheet was observed from the top of bottom foundation with a distance of 280 mm. The failure mode of RW1 was shown in **Fig. 10**. As shown in the figure, severe CFRP dobonding was observed at the lower part of the wall. After cutting of partial of CFRP laminates, severe concrete spalling was observed. At the corner of the wall, severe concrete crushing with buckling of replaced rebar was observed.

4.1.2 RW2

Similar to RW1, before reaching DR of 0.75 %, no crack and CFRP debonding occurred. At DR of 0.75 %, the lower part of the diagonal strip began to debond slightly and sound due to debonding was heard. At DR of 1.0 %, the lowest horizontal wrapping began to debond. Further increase of the DR to 1.5 %, C-shaped CFRP sheets at the corner of the wall began to form bulk, which means severe concrete crushing at there. At DR of 1.75 %, the lowest horizontal wrapping strips and diagonal sheet debonded severely and the debonding zones were connected. Further increase the DR to 2.25 %, the middle part of the horizontal wrapping delaminated completely, and severe concrete crushing occurred at the corner of the wall. **Fig. 11** shows the failure mode of Specimen RW2. In general, it was very similar to that of RW1. Severe concrete spalling and crushing were observed at the lower part of the wall. Completely delaminating was observed at lower part of the diagonal strips. CFRP bulk and rebar buckling was observed at both corner of the wall after severe concrete crushing.

4.1.3 RW3

Similar to RW1 and RW2, the debonding was first observed at the diagonal strip at a DR of 0.75 %. At a DR of 1.0 %, debonding was also occurred at the lowest horizontal wrapping. Slight debonding was observed at C-shaped sheet at DR of 1.25 %. Concrete crushing at the corner of the wall was observed at DR of 1.5 %. Further increase of DR, more concrete crushing and debonding was observed. The failure mode of Specimen RW3 is shown in **Fig. 12**. As shown in the figure, the concrete spalling at the front face of the wall was also milder. Moreover, the debonding of C-shaped sheets and concrete crushing at the wall corner was much milder. This could be explained by the fractured or buckling rebar was not replaced. There was the demand of compressive force from concrete was less when flexure strength was considered.

4.1.4 RW4

Different to above three specimens, RW4 was repaired by CFRP rehabilitation scheme 2. Debonding of CFRP was observed at the right vertical strip at DR of 0.5 %, which was earlier than above three specimens. Tearing was observed at the right vertical strip at DR of 0.75 %. At DR of 1.0 %, debonding was also observed at the lowest horizontal wrapping strips. At DR of 1.25 %, middle vertical strips began to debond and the debonding of the lowest horizontal wrapping strip becomes more severe. Further increase the DR to 1.5 %, CFRP bulk becomes more obvious at the corner of the wall, which means concrete crushing becomes more severe. Further increasing DR to 2.0 %, the debonding zone at the lower part of the wall connected and CFRP strips at the lower part of the wall quit work. **Fig. 13** shows the failure mode of Specimen RW4. As shown in the figure, severe delaminating was observed at the lower part of the wall. Similar to RW3, concrete crushing was much milder than that of RW1 and RW2.

4.2. Load-displacement hysteresis responses

Fig. 14 illustrates the comparison of load-displacement hysteresis loops of the control and repaired specimens. As shown in **Fig. 14a** and **Table 4**, in general, the lateral load resistance of RW1 was slightly less than that of control specimen SW1 in terms of positive and negative directions. The average yield load of the Control Specimen SW1 was 284.3 kN while the yield load of Repaired Specimen RW1 was 275.3 kN, which was 97 % of that of SW1. In addition, the average peak load of the Control Specimen SW1 and Repaired Specimen RW1 were 348.7 kN and 317.3 kN, respectively. Therefore, replacing the buckling rebar and CFRP repairing scheme 1 could recover the lateral load of SW1 well. For SW2 and RW2, the average yield load was 287.5 kN and 273.0 kN, respectively. Therefore, replacing the buckling rebar and applying scheme 1 could recovery the yield load by 95 % (refer to **Fig. 14b**). Similarly, regarding average peak load, RW2 recovered about 89 %, which was less than that of yield load. As shown in **Table 4** and **Fig. 14c**, the average yield load and peak load of RW3 was 89 % and 91 % of that of SW3, respectively. Therefore, although the buckled rebar was not replaced, CFRP scheme 1 could recover the lateral load resistance well. However, comparing to RW3, as shown in **Fig. 14d**, RW4 only recovered the yield load and peak load by 73 % and 79 %, respectively. Therefore, CFRP scheme 2 was less effective than that of scheme 1 in terms of lateral load resistance. However, if we look at the shape of hysteresis loops, both control specimens and repaired specimen performed ductile. Actually, the repaired specimens even have less pinching. Moreover, the strength degradation of repaired specimens also slower than that of corresponding controlled specimens. As shown in the figure, when DR exceeded 1.5 %, the load resistance of RW1 and RW2 was larger than SW1 and SW2. For RW3 and RW4, the repaired specimens could exceed the load resistance of SW3 and SW4 after DR of 2.0 %.

4.3. Strength degradation

Figs. 15 to **18** present the strength degradation of tested specimens. As shown in **Fig. 15**, for both 2^{nd} and 3^{rd} cycles, the factor of strength degradation of RW1 was larger than that of SW1. This means replacing buckled rebar and CFRP scheme 1 could restore the strength degradation well. For RW2 and RW3, the factor of strength degradation of repaired specimens varied along the factor of corresponding control specimen. Therefore, in general, RW2 and RW3 could obtain similar strength degradation behavior of the control specimens. However, for RW4, as shown in **Fig. 18**, the factor of strength degradation both in the 2^{nd} and 3^{rd} cycles of repaired specimen were less than that of control specimen SW4. This further confirmed that the rehabilitation efficiency of scheme 2 was less than that of scheme 1.

4.4. Stiffness degradation

Fig. 19 shows the comparison of the stiffness degradation of control and repaired specimens. It should be noted that secant stiffness, the ratio of lateral load to corresponding displacement, was determined in the figure. As shown in **Fig. 19a**, the initial stiffness of SW1 and RW1 in positive direction was 55.3 kN/mm and 39.7 kN/mm, respectively. Therefore, RW1 recovered the initial stiffness by 71.8 %. However, the stiffness degradation of SW1 was faster than RW1 and thus, when DR exceeded 1.5 %, the stiffness of RW1 was greater than that of SW1. Similarly, the initial stiffness of SW2 and RW2 in positive direction was 56.3 kN/mm and 51.5 kN/mm, respectively. Thus, RW2 recovered the initial stiffness by 91.5 %. Moreover, RW3 and RW4 recovered the initial stiffness of SW3 and SW4 by 76.1 % and 74.3 %, respectively. Moreover, when DR exceeded 2.0 %, the stiffness of RW3 and RW4 was larger than SW3 and SW4.

The stiffness of both the control and repaired walls was calculated using the secant stiffness of the plots of force against displacement. **Fig.19** shows the comparisons of stiffness degradation for each tested specimen. The comparison of the Repaired Specimen RW1 curve with the corresponding curve for Control Specimen SW1 shows that the initial stiffness of Specimen RW1 was significantly higher than that of Specimen SW1. The Repaired Specimen RW1 was not as stiff as the original wall in considering the negative loading cycles while, generally speaking, the Repaired Specimen RW1 had recovered the stiffness reasonably. On the other hand, the Repaired Specimen RW2 not only had much higher initial stiffness but also had delayed stiffness degradation compared with the corresponding control Specimen SW2. This is a desirable property in an earthquake-like situation. It was observed, in the past earthquake, that most of the RC structures failed due to the sudden loss of stiffness of structural joints with increasing lateral movement of the structure.

4.5. Energy dissipation capacity

Fig. 20 gives the comparison of the energy dissipation capacity, which was determined based on the summation of the energy dissipated in consecutive loops throughout the test. As shown in the figure, the curves of repaired specimens were lower than that of corresponding control specimen from the beginning of the test. As tabulated in **Table 4**, the total dissipated energy of SW1, RW1, SW2, RW2, SW3, RW3, SW4, and RW4 were 445.9 kN.m, 366.9 kN.m, 353.1 kN.m, 312.4 kN.m, 336.1 kN.m, 329.4 kN.m, 372.5 kN.m, and 301.4 kN.m, respectively. Therefore, RW1, RW2, RW3, and RW4 recovered the dissipated energy by 82 %, 88 %, 98 %, and 81 %, respectively.

4.6. De-composition of the lateral displacement

The lateral displacement at the loading point consisted of two main components shear deformation and flexural deformation. Data captured by LVDTs mounted on the specimens were used to de-composite the contribution of each source, following the procedures described by Zhang et al.[16]. In general, the total summed lateral displacement was larger than the measure one. However, the difference was less than 5 %. **Fig. 20** shows the comparison of the de-composition of lateral displacement in accord with different DR. For SW1, majority of the deformation was attributed into the flexural bending. However, the contribution of shear deformation kept increasing with the increase of DR. At DR of 0.25 % and 2.0 %, the flexural component was about 84.1 % and 75.0 %, respectively. This agreed with the failure mode of the specimen well. Actually, flexural-shear failure controlled the failure mode.

For RW1, similar to that of SW1, flexural component dominated the lateral deformation. However, comparing to SW1, the contribution of shear component was increased. As shown in **Fig. 20b**, the shear component increased from 14.1 % to 36.2 % when DR increased from 0.25 % to 2.0 %. This could be explained as the repairing schemes were designed mainly for restoring the flexural strength. The initial damage of shear failure was not repaired well in this study.

5. Discussion of the efficiency of repairing schemes

As shown in **Figs. 10**and **11**, replacing the buckled rebar and applied CFRP scheme 1 resulted in severe concrete crushing at the bottom corner of the walls as well as severe tearing of CFRP sheet at both sides. However, as shown in **Fig. 12**, if we did not replace the buckled rebar but only applied CFRP scheme 1, the concrete crushing and tearing of CFRP was less severer which was mainly due to less compressive stress required. However, comparison of **Figs. 12** and **13**, RW4, which was retrofitted by CFRP scheme 2 but without replacing buckled rebar, has more severe debonding of CFRP strips and more severe of concrete crushing and tearing of CFRP sheet at bottom corner of the wall.

Comparison of the backbone curve of repaired specimen with corresponding control specimen, as shown in **Fig. 22**, indicated that RW1 and RW2 could recover the behavior of control specimen SW1 and SW2 reasonable in terms of lateral load resistance, initial stiffness, and ultimate deformation capacity. Conversely, RW3 and RW4 could not recover the behavior of corresponding control specimens, especially for the initial stiffness, yield load, and peak load capacity. Comparing RW3 with RW4, it was found that scheme 1 seems more effective. However, it should be noted that more tests on repairing or strengthening steel-concrete composite walls should be carried out in the future to find more effective repairing or strengthening schemes.

5. Conclusions

The behavior of the steel-concrete composite walls with or with prestressed internal bracing subjected to repeated lateral displacements were investigated in the present study. The seismically damaged walls were repaired by replacing buckled rebar with different CFRP repairing schemes or CFRP repairing schemes alone . Then, the repaired specimens were compared with that control specimen. The following conclusions were drawn from the results.

1. The X-shaped prestressed bracing could delay the form of first crack. However, regarding the yield load and peak load, X-shaped prestressed bracing has little effects.

2. The experimental results presented in this study indicated that replacing buckled rebar and proper CFRP schemes could recover lateral load resistance and stiffness reasonably well. However, if buckled rebar was not replaced, proposed CFRP repairing schemes could not recover initial stiffness and peak load resistance well. However, even only applying CFRP schemes, the lateral load resistance in large deformation stage could be recovered.
3. The ratio of yield load, peak load, energy dissipation capacity of repaired specimens with corresponding control specimens indicated that CFRP scheme 1 was more effective than that of CFRP scheme 2.

Authors' contributions

Dr. Kai Qian gives idea for the study, Dr. Jin-Fang Sun carried out experimental tests. All authors analyzed the data and were involved in writing the manuscript.

Conflict of interest

The authors declare that there is no conflict of interest regarding the publication of this paper.

Acknowledgements

The authors gratefully acknowledge the financial support provided by the Natural Science Foundation of China (Nos. 51778153, 51568004, 51478118). Any opinions, findings and conclusions expressed in this paper do not necessary reflect the view of Natural Science Foundation of China.

References

[1] W. Lan, J. Ma, B. Li, Seismic performance of steel-concrete composite structural walls with internal bracings, Journal of Constructional Steel Research 110 (2015) 76-89.
[2] H.D. Wright, S.C. Gallocher, The behavior of composite walling under construction and service loading, Journal of Constructional Steel Research. 35 (3) (1995)257-273.
[3] H. D. Wright, The axial load behavior of composite walling, Journal of Constructional Steel Research. 45 (3) (1998)353-375.
[4] K. Emori, Compressive and shear strength of concrete filled steel box wall, Steel Structures 68(2) (2002) 29–40.

[5] D. Dan, A. Fabian, V. Stoian, Theoretical and experimental study on composite steel-concrete shear walls with vertical steel encased profiles, Journal of Constructional Steel Research. 67 (5) (2011)800-813.

[6] D. Dan, A. Fabian, V. Stoian, Nonlinear behavior of composite shear walls with vertical steel encased profiles, Engineering Structures. 33 (10) (2011)2794-2804.

[7] W. Lan, J. Ma, B. Li, Seismic performance of steel-concrete composite structural walls with internal bracing, Journal of Constructional Steel Research. 110 (2015)76-89.

[8] W. Lan, Z. Zhang, B. Li, Seismic performance of T-shaped steel-concrete composite structural walls subjected to loadings from different directions, Journal of Constructional Steel Research. 128 (2017)7-18.

[9] L. Tie-jiong, S.M.R. Lopes, A.V. Lopes, Numerical modeling of externally prestressed steel – concrete composite beams, J. Constr. Steel Res. 121 (6) (2016) 229-236.

[10] F.X. Ding, J. Liu, X. M. Liu, Z.W. Yu, Y.S. Li, Experimental investigation on hysteretic behavior of simply supported steel-concrete composite beam, J. Constr. Steel Res. 144 (2018) 153-163.

[11] M.Z. Wang, Y.L. Guo, J.S. Zhu, X. Yang, J.Z. Tong, Sectional strength design of concrete-infilled double steel corrugated-plate walls with T-section, J. Constr. Steel Res. 160(2019) 23-44.

[12] Y.Qin, G.P. Shu, G.G. Zhou, J.H. Han, Compressive behavior of double skin composite wall with different plate thickness, J. Constr. Steel Res. 157(2019) 297-313.

[13] B.L. Lai, J.Y.R. Liew, T.Y. Wang, Buckling behavior of high strength concrete encased steel composite columns, J. Constr. Steel Res. 154(2019) 27-42.

[14] M. Engindeniz, L.F. Kahn, A.H. Zureick, Repair and strengthening of reinforced concrete beam-column joints: state of the art, ACI Structural Journal 102(2) (2005) 187-197.

[15] B. Li, K. Qian, C.T.N. Tran, Retrofitting earthquake-damaged RC structural walls with openings by externally bonded FRP strips and sheets, Journal of Composites for Construction, 17(2)(2012) 259-270.

[16] Z.W. Zhang, B. Li, K. Qian, Experimental investigations on seismically damaged nonrectangular reinforced-concrete structural walls repaired by FRPs, Journal of Composites for Construction. 20(1) (2016) 04015033.

[17] C. Popescu, G. Sas, T. Blanksvard, B. Taijsten, Concrete walls weakened by openings as compression members: a review, Engineering Structures, 89(2015) 172-190.

[18] C. Popescu, G. Sas, C. Sbau, T. Blanksvard, Effect of cut-out openings on the axial strength of concrete walls, Journal of Structural Engineering, 142(11)(2016) 04015033.

[19] M. Lima, J. Doh, M. Hadi, Experimental study on RC walls with opening strengthened by externally bonded CFRP, Journal of Composites for Construction, 23(2) (2019) 04019008.

[20] B. Li, C.L. Lim, Tests on seismically damaged reinforced concrete structural walls repaired using fiber-reinforced polymers, Journal of Composites for Construction 14(5) (2010) 597-608.

[21] Q.H. Shen, J.F. Wang, J.X.Wang, Z.D. Ding, Axial compressive performance of circular CFST columns partially wrapped by carbon FRP, Journal of Constructional Steel Research, 155 (2019) 90-106.

[22] E. Katrizadeh, K. Narmashiri, Experimental study on failure modes of MF-CFRP strengthened steel beams, Journal of Constructional Steel Research, 158 (2019) 120-129.

[23] M. Altaee, L.S. Cunningham, M. Gillie, Practical application of CFRP strengthening to steel floor beams with web openings: a numerical investigation, Journal of Constructional Steel Research, 155 (2019) 395-408.

[24] E.A. Amoush, M. A. Ghanem, Axially loaded capacity of alternatively strengthened cold-formed channel columns with CFRP, Journal of Constructional Steel Research, 140 (2018) 139-152.

[25] W. W. Lan, B. Li, Z. W. Zhang, Seismic performance of steel-concrete composite structural walls with prestressed internal bracing, Journal of Constructional Steel Research, 140 (2018) 11-24.

Table 1 Property of test specimens

Test ID	Reinforcement Ratio (%)			Embedded Steel Ratio	Post-tension Force (kN)	Internal Bracing	Repair Scheme	Rebar Replace
	Horizontal	Vertical	Volume Ratio					
SW1	0.59	1.27	1.34	3.17	N/A	N/A	N/A	N/A
SW2	0.59	1.27	1.34	3.17	110	PVC Duct	N/A	N/A
SW3	0.59	1.27	1.34	3.17	126	PVC Duct	N/A	N/A
SW4	0.59	1.27	1.34	3.17	110	Steel Tube	N/A	N/A
RW1	0.59	1.27	1.34	3.17	N/A	N/A	A	Yes
RW2	0.59	1.27	1.34	3.17	N/A	No Repair	A	Yes
RW3	0.59	1.27	1.34	3.17	N/A	No Repair	A	No
RW4	0.59	1.27	1.34	3.17	N/A	No Repair	B	No

Table 2 Properties of reinforcements and shaped steel

	Yield Strength (N/mm^2)	Ultimate Strength (N/mm^2)	Young's Modulus (N/mm^2)
T10	468	642	2.05×10^5
R6	382	526	2.08×10^5
Tensile Threaded Rod (20 mm)	575	705	1.90×10^5
L30 × 3 Angle Steel	333	413	2.02×10^5
80 × 43× 5C Shaped Steel	362	559	2.03×10^5
40 × 30× 3 Rectangular Steel Tube	346	493	2.02×10^5

Note: T10 and R6 represent deformed rebar with diameter of 10 mm and plain rebar with diameter of 6 mm, respectively.

Table 3 Properties of CFRP composite system

Parameters	Properties
Type of FRP	Unidirectional CFRP sheet
Ultimate tensile strength in primary fiber direction	3680 MPa
Elongation at break	1.6 %
Tensile Modulus	225×10^3 MPa
Laminate thickness	0.167 mm

Table 4 Comparison of the critical results

	SW1	SW2	SW3	SW4	RW1	RW2	RW3	RW4	RW1/ SW1	RW2/ SW2	RW3/ SW3	RW4/ SW4
First Crack Load (kN)	126.5	164	180	160	70.6	98.1	126.0	107.6	0.56	0.60	0.70	0.67
First Crack Displacement (mm)	1.18	1.38	2.19	1.76	1.71	1.91	1.93	1.92	1.45	1.38	0.88	1.09
Yield Load (kN)	284.3	287.5	285.9	307.2	275.3	273.0	253.7	223.3	0.97	0.95	0.89	0.73
Displacement at Yield Load (mm)	5.7	5.5	6.1	7.3	11.5	9.0	12.2	10.1	2.02	1.64	2.00	1.38
Peak Load (kN)	348.7	354.8	351.5	368.5	317.3	315.3	318.2	289.9	0.91	0.89	0.91	0.79
Displacement at Peak Load (mm)	11.0	11.5	11.5	14.8	23.0	20.8	30.2	19.1	2.09	1.81	2.63	1.29
Secant Stiffness at Yield Load (kN/mm)	49.9	52.3	46.9	42.1	23.9	30.3	20.8	22.1	0.48	0.58	0.44	0.52
Total Energy Dissipation (kN·m)	445.9	353.1	336.1	372.5	366.9	312.4	329.4	301.4	0.82	0.88	0.98	0.81

List of Figures

Fig. 9 Strengthening Scheme 2: (a) drawing, (b) photo

Fig. 10 Failure mode of repaired specimen RW1: (a) before cutting FRP strips, (b) after removal of partial of CFRP strips

Fig. 11 Failure mode of repaired specimen RW2: (a) before cutting FRP strips, (b) after removal of partial of CFRP strips

Fig. 12 Failure mode of repaired specimen RW3: (a) front view, (b) side view

Fig. 13 Failure mode of repaired specimen RW4: (a) front view, (b) side view

Fig. 14 Hysteresis response of control and repaired specimens

Fig. 15 Comparison of the strength degradation of SW1 and RW1: (a) 2nd cycle, (b) 3rd cycle

Fig. 16 Comparison of the strength degradation of SW2 and RW2: (a) 2nd cycle, (b) 3rd cycle

Fig. 17 Comparison of the strength degradation of SW3 and RW3: (a) 2nd cycle, (b) 3rd cycle

Fig. 18 Comparison of the strength degradation of SW4 and RW4: (a) 2nd cycle, (b) 3rd cycle

Fig. 19 Comparison of the stiffness degradation of tested specimens

Fig. 20 Comparison of the energy dissipated capacity of tested specimens

Fig. 21 Decomposition of the displacement: (a) SW1, (b) RW1

Fig. 22 Comparison of the envelop of the control and repaired specimens

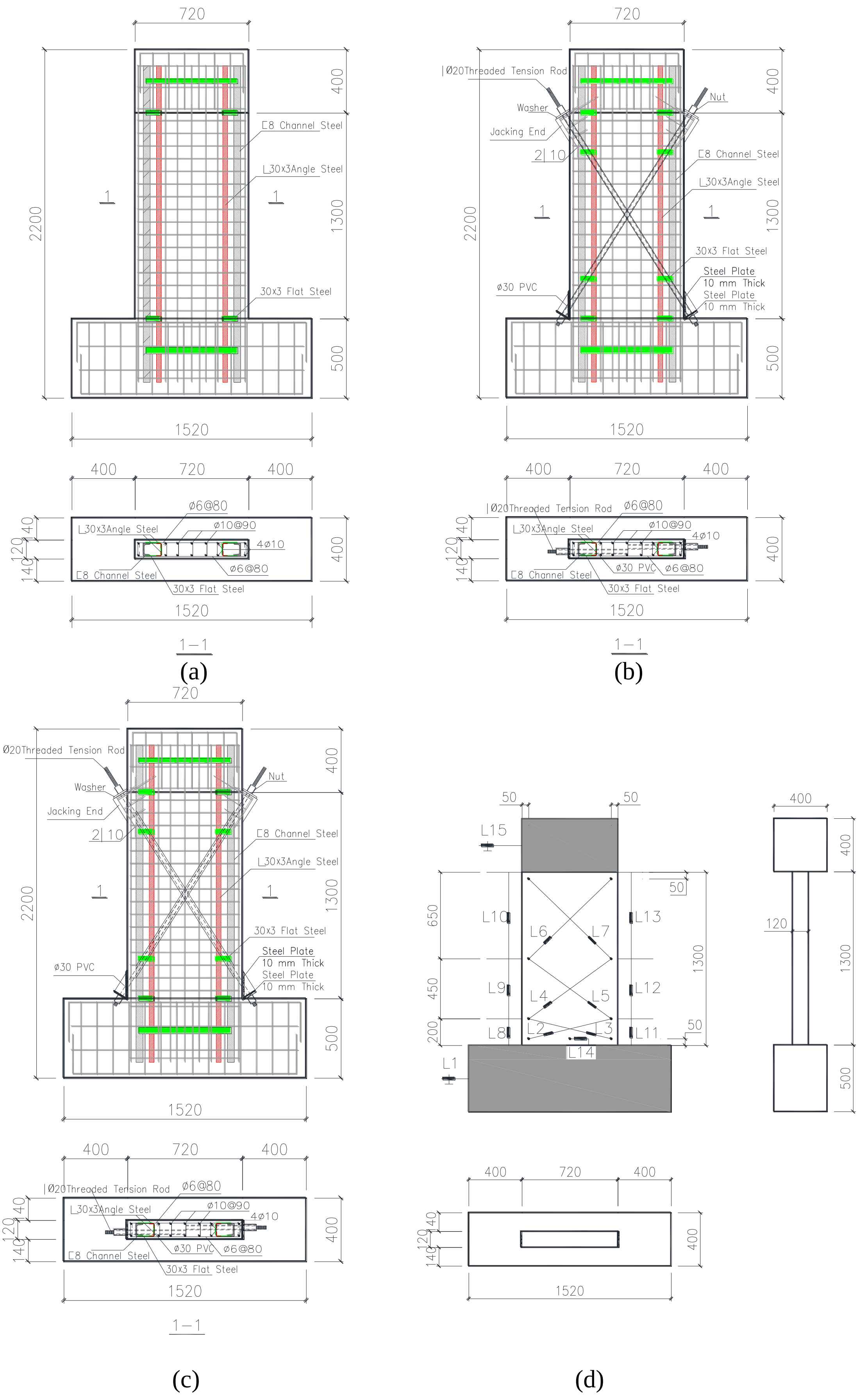

Fig. 1 Dimensions and reinforcement details as well as instrumentations: (a) SW1, (b) SW2&SW3, (c) SW4, and (d) instrumentation layout

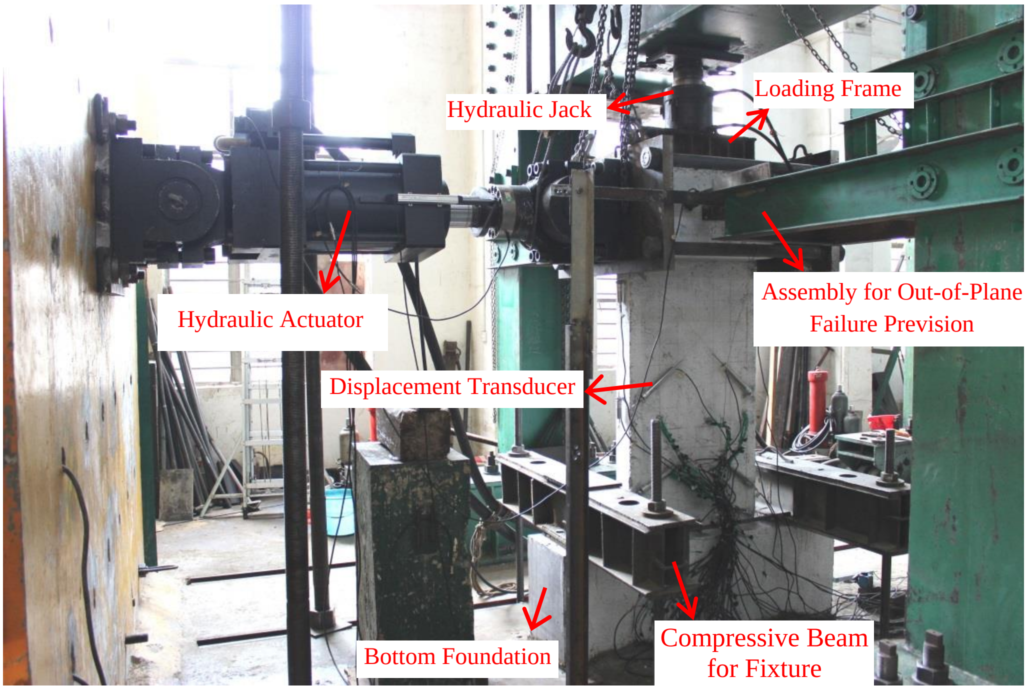

Fig. 2 Specimen SW1 before testing

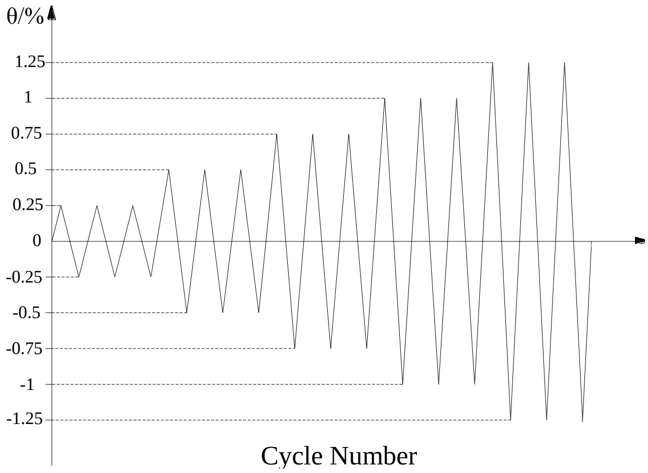

Fig. 3 Typical loading procedure

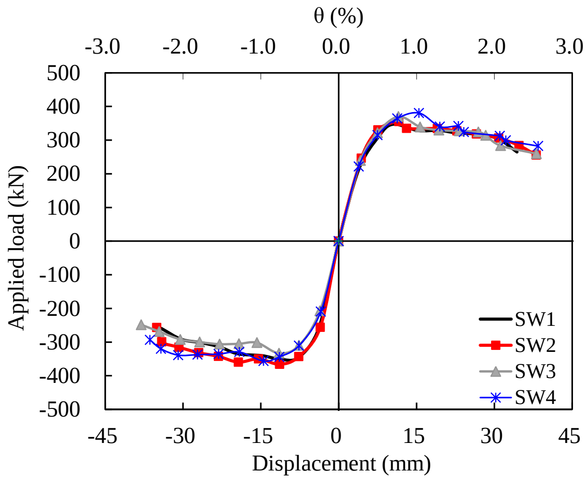

Fig. 4 Comparison of the backbone curve of control specimens

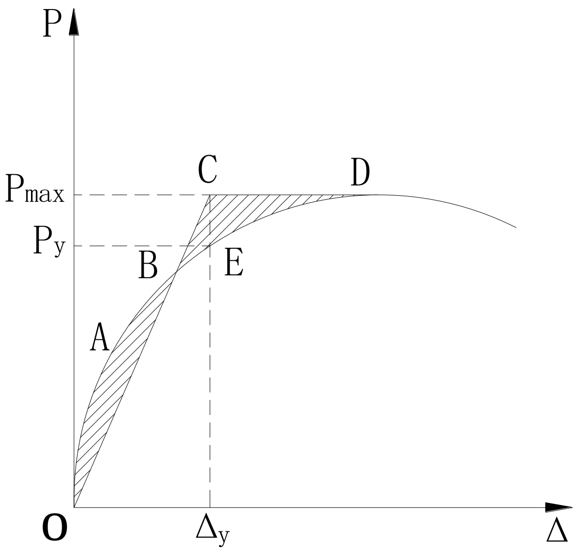

Fig. 5 Definition of the yield point by energy equilibrium method

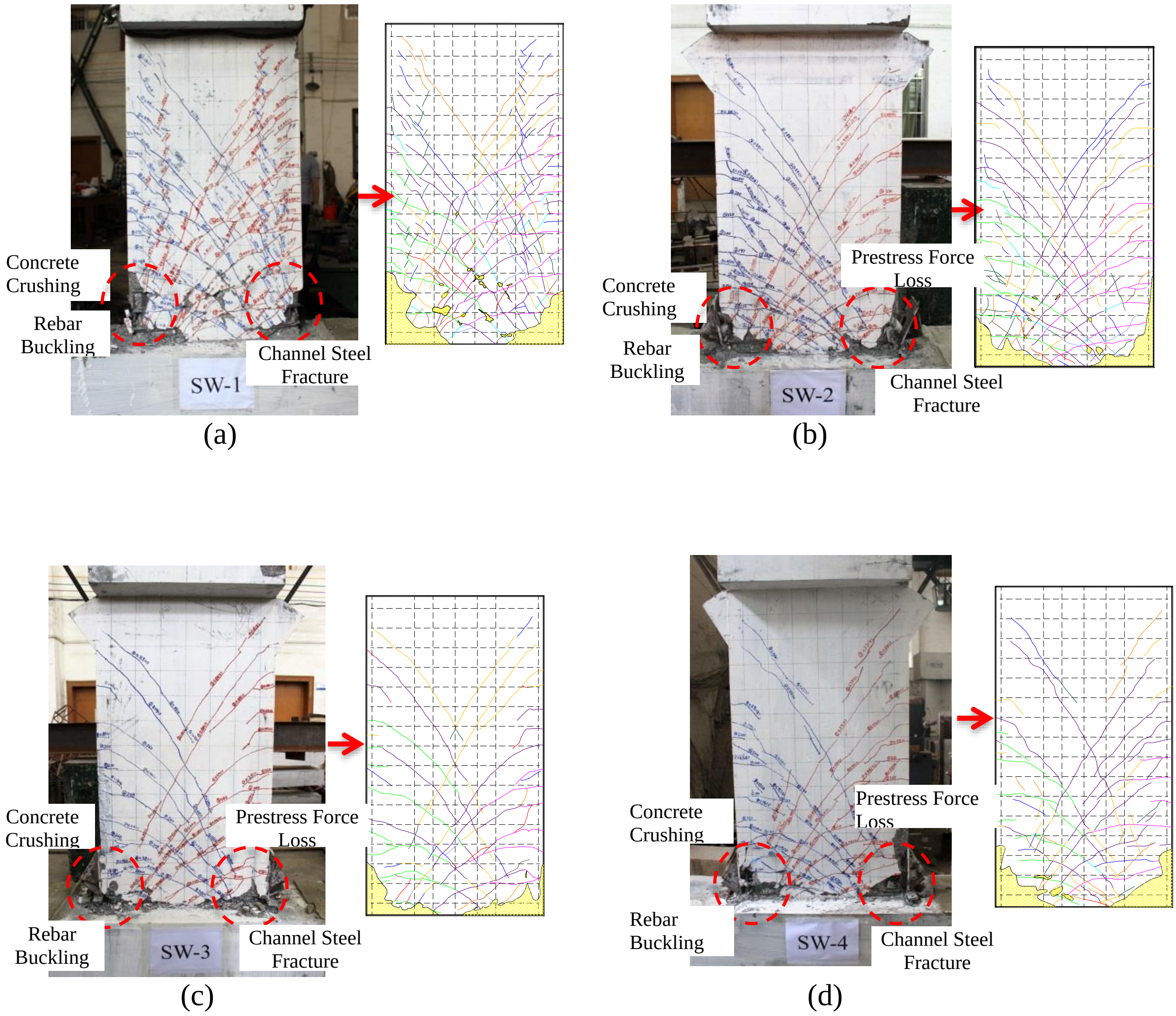

Fig. 6 Failure mode of control specimens: (a) SW1, (b) SW2, (c) SW3, and (d) SW4

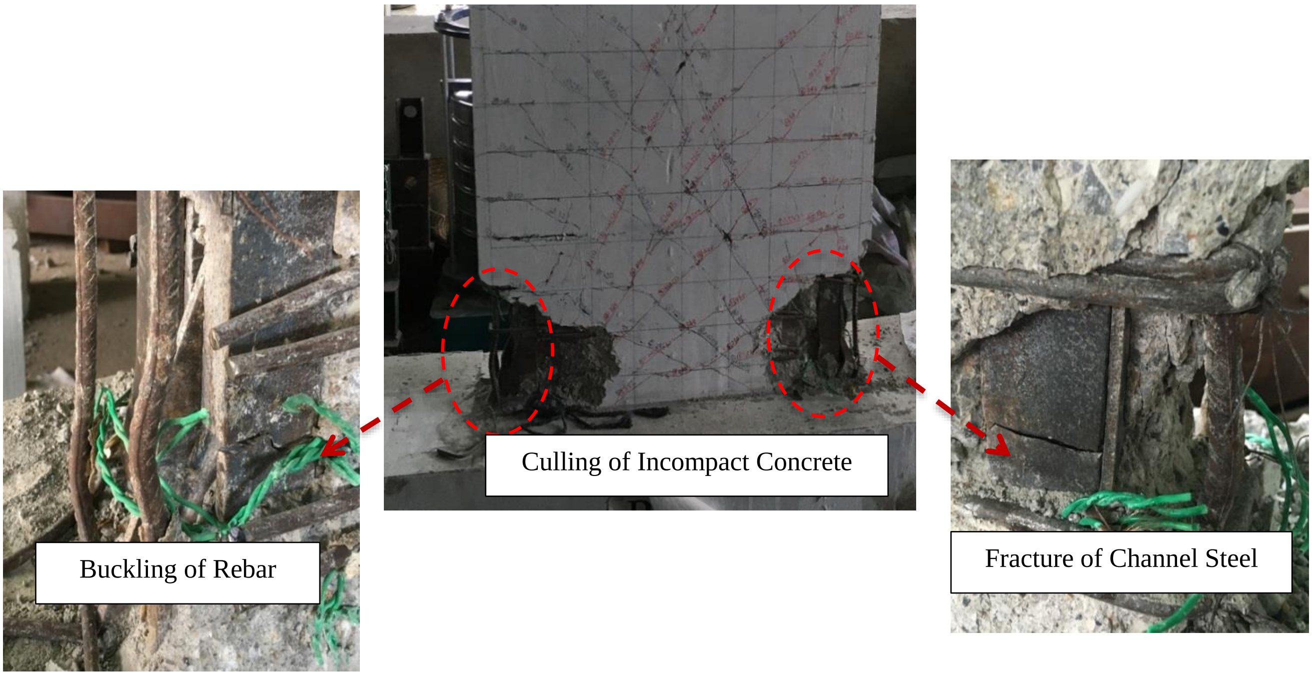

Fig. 7 Typical failure mode of the specimen after culling of incompact concrete

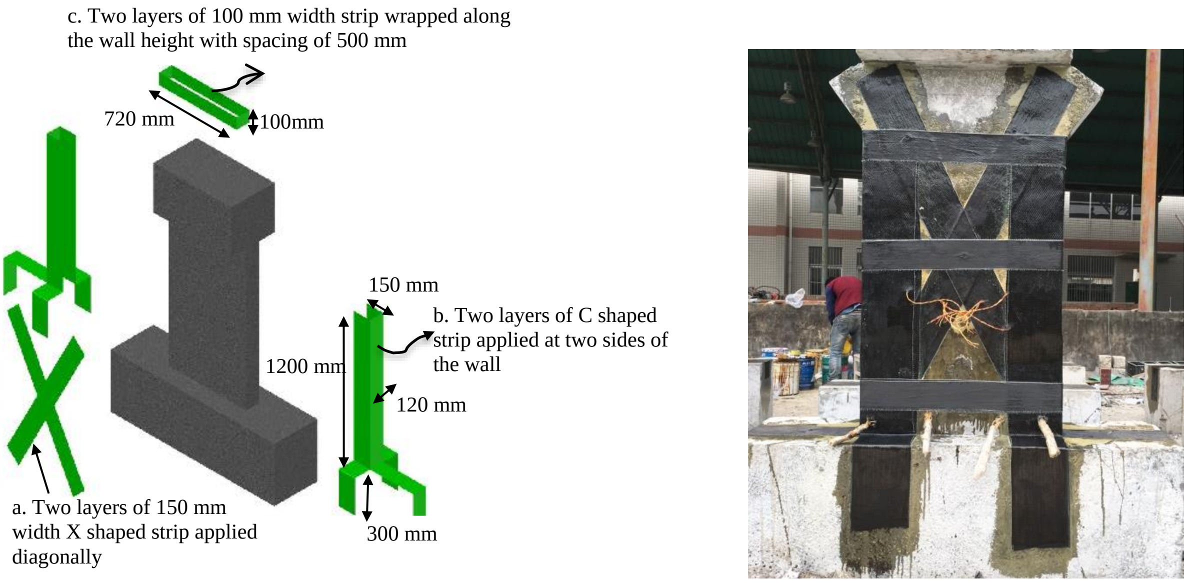

(a) (b)

Fig. 8 Strengthening Scheme 1: (a) drawing, (b) photo

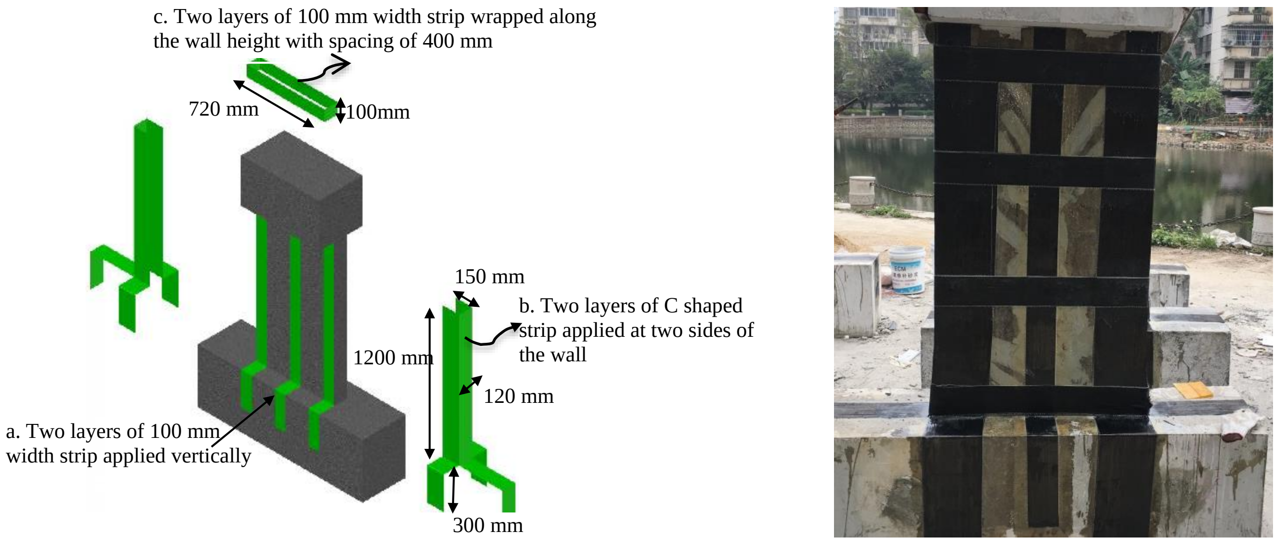

Fig. 9 Strengthening Scheme 2: (a) drawing, (b) photo

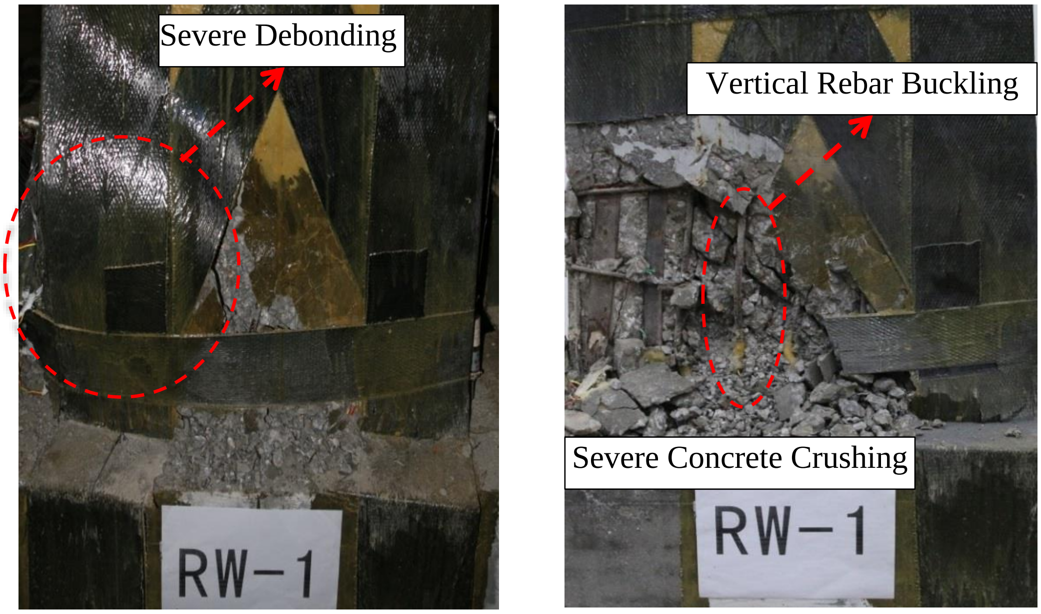

(a) (b)

Fig. 10 Failure mode of repaired specimen RW1: (a) before cutting FRP strips, (b) after removal of partial of CFRP strips

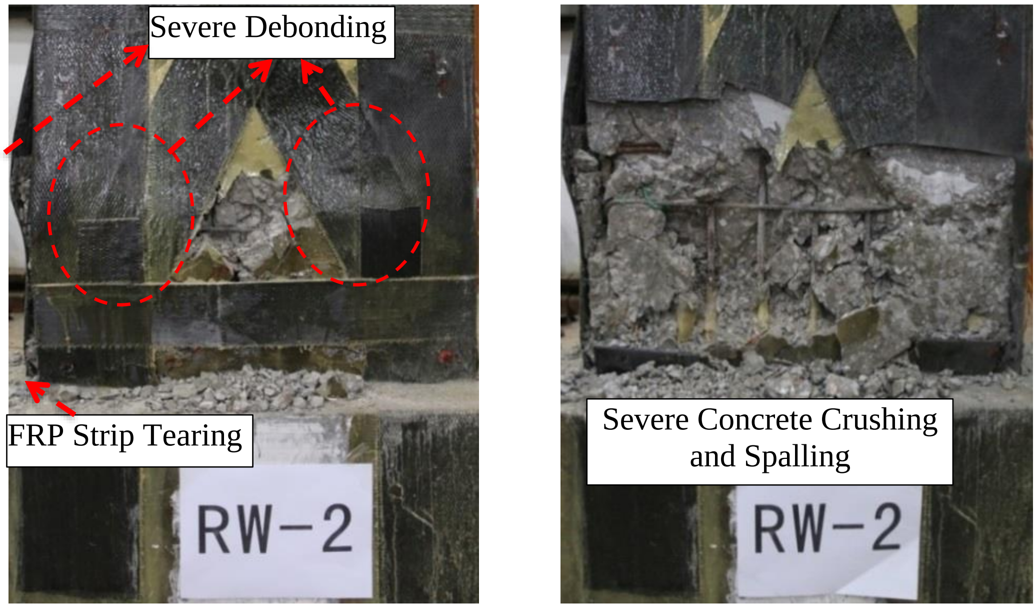

(a) (b)

Fig. 11 Failure mode of repaired specimen RW2: (a) before cutting FRP strips, (b) after removal of partial of CFRP strips

(a) (b)

Fig. 12 Failure mode of repaired specimen RW3: (a) front view, (b) side view

(a) (b)

Fig. 13 Failure mode of repaired specimen RW4: (a) front view, (b) side view

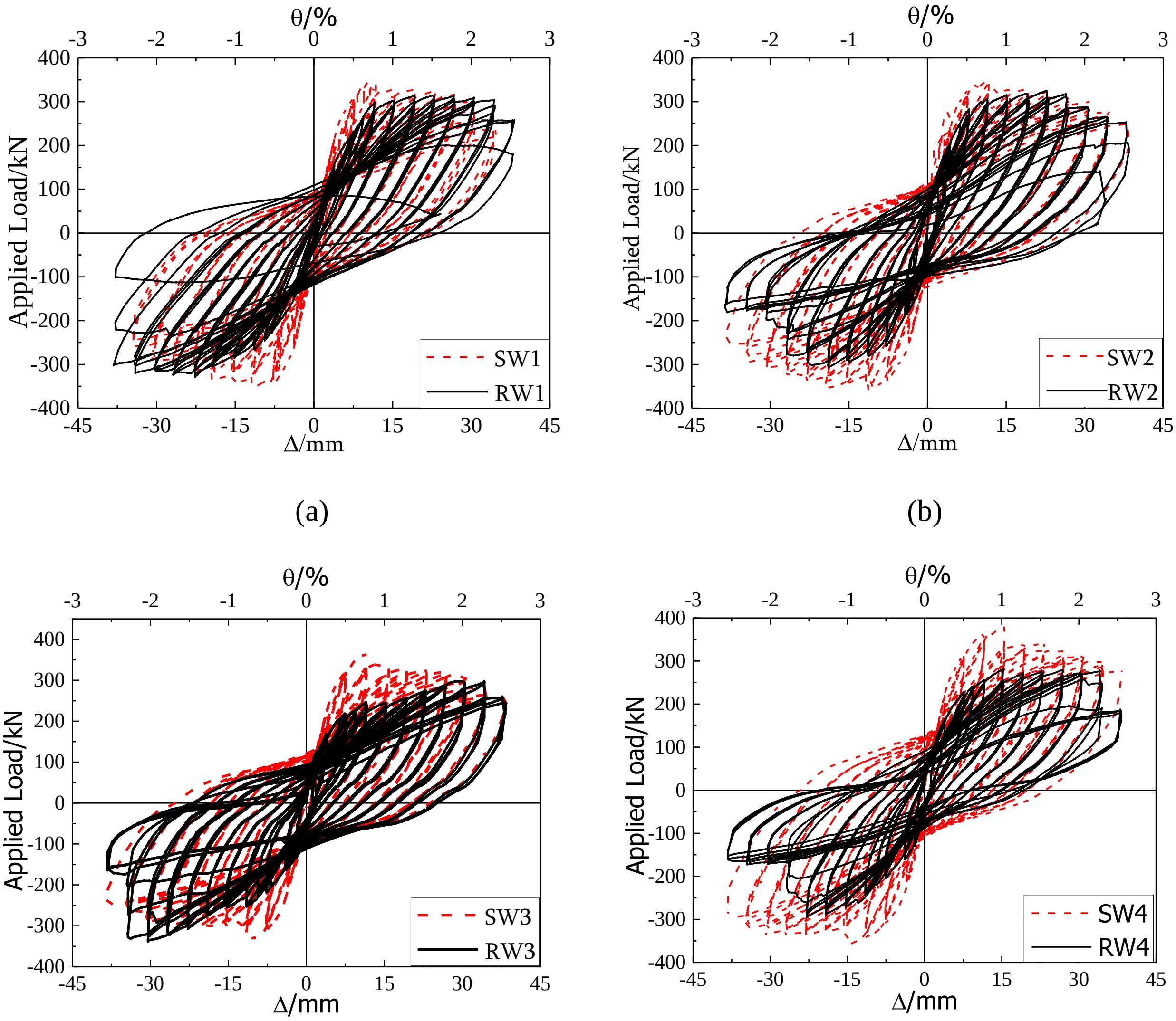

(a) (b)

(c) (d)

Fig. 14 Hysteresis response of control and repaired specimens

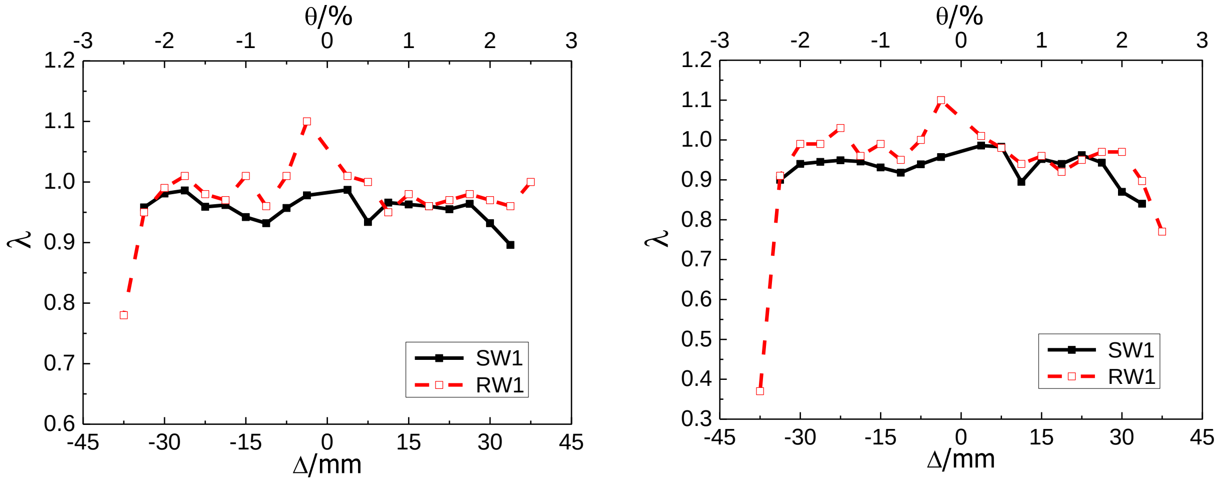

(a) (b)

Fig. 15 Comparison of the strength degradation of SW1 and RW1: (a) 2nd cycle, (b) 3rd cycle

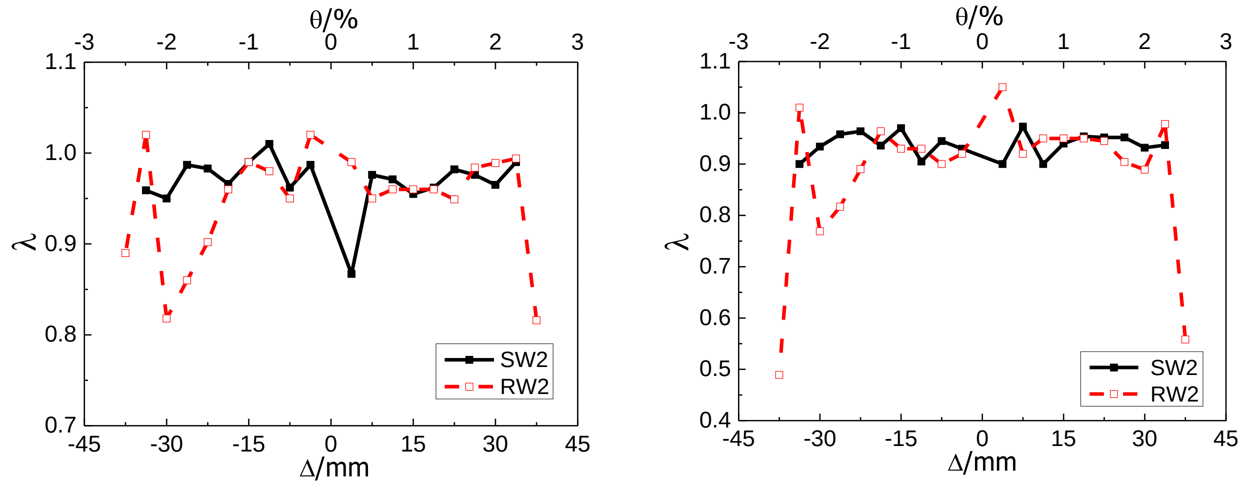

(a) (b)

Fig. 16 Comparison of the strength degradation of SW2 and RW2: (a) 2nd cycle, (b) 3rd cycle

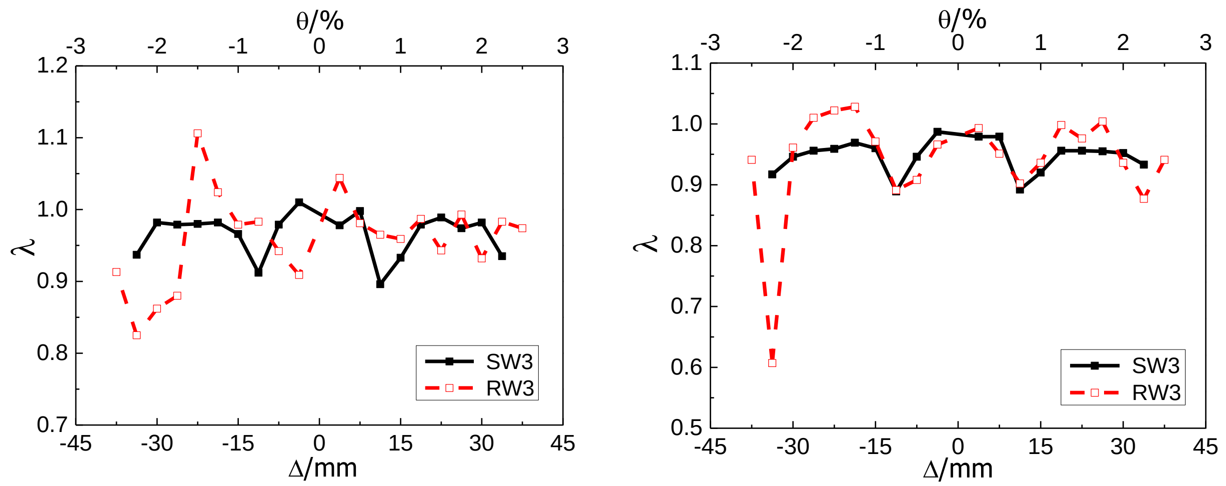

(a) (b)

Fig. 17 Comparison of the strength degradation of SW3 and RW3: (a) 2nd cycle, (b) 3rd cycle

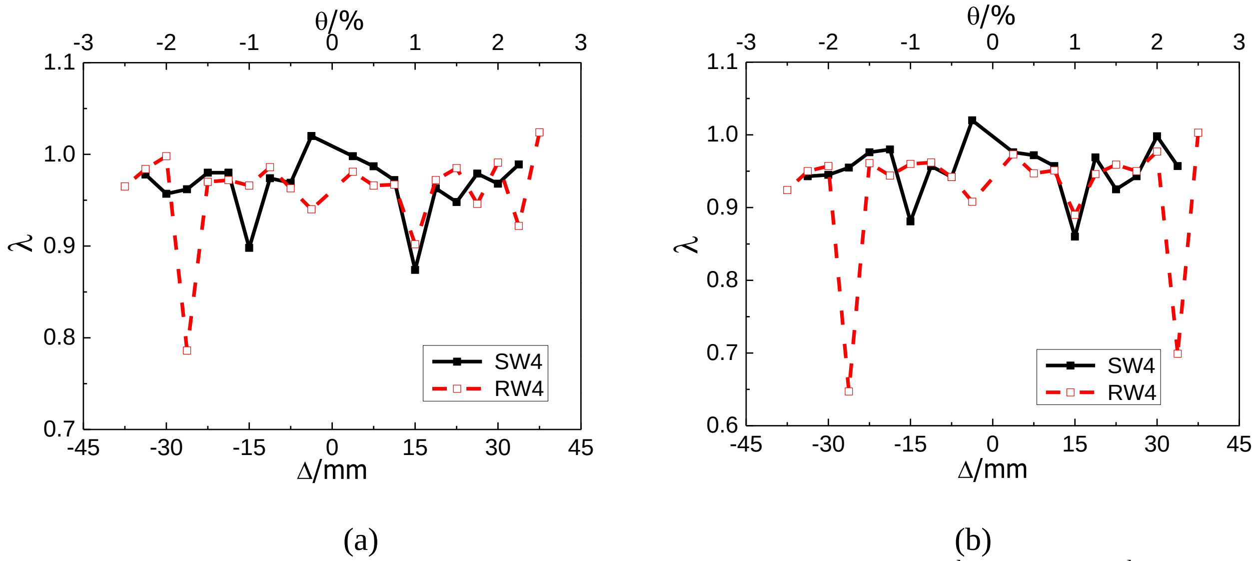

Fig. 18 Comparison of the strength degradation of SW4 and RW4: (a) 2nd cycle, (b) 3rd cycle

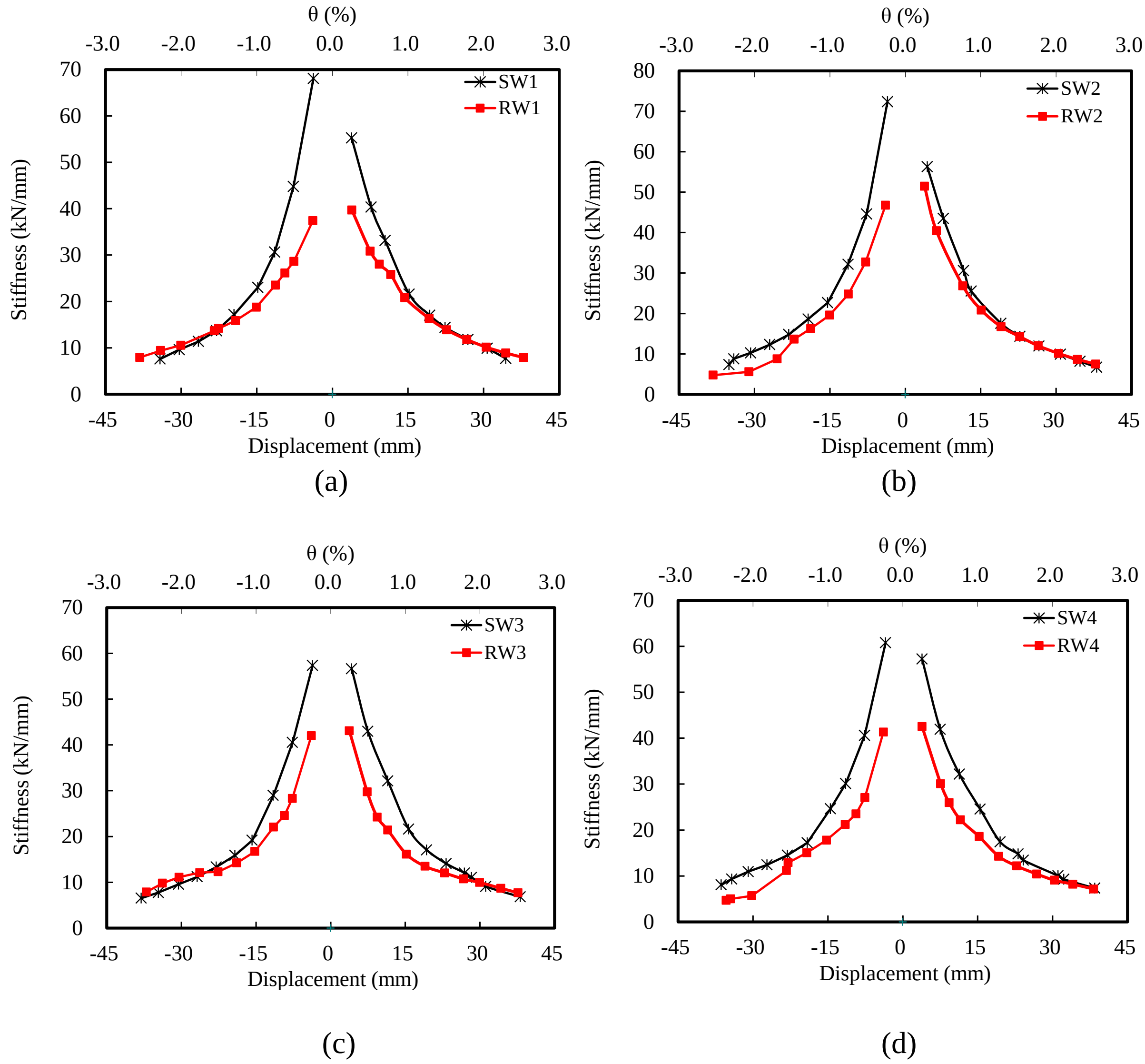

Fig. 19 Comparison of the stiffness degradation of tested specimens

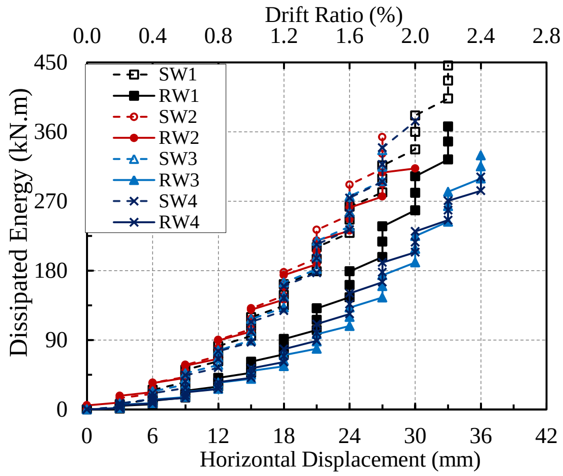

Fig. 20 Comparison of the energy dissipated capacity of tested specimens

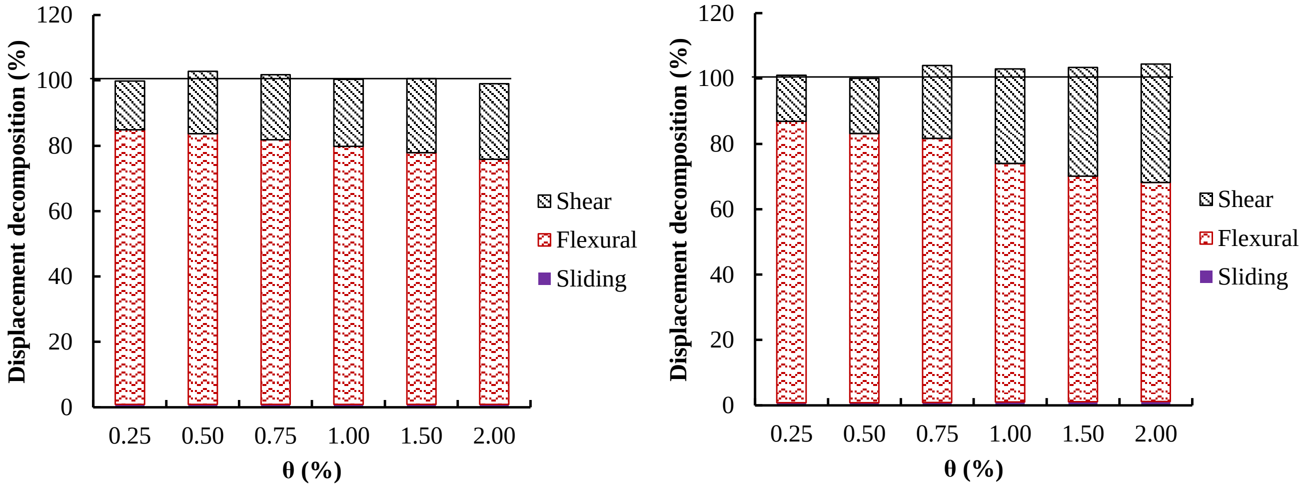

(a) (b)

Fig. 21 Decomposition of the displacement: (a) SW1, (b) RW1

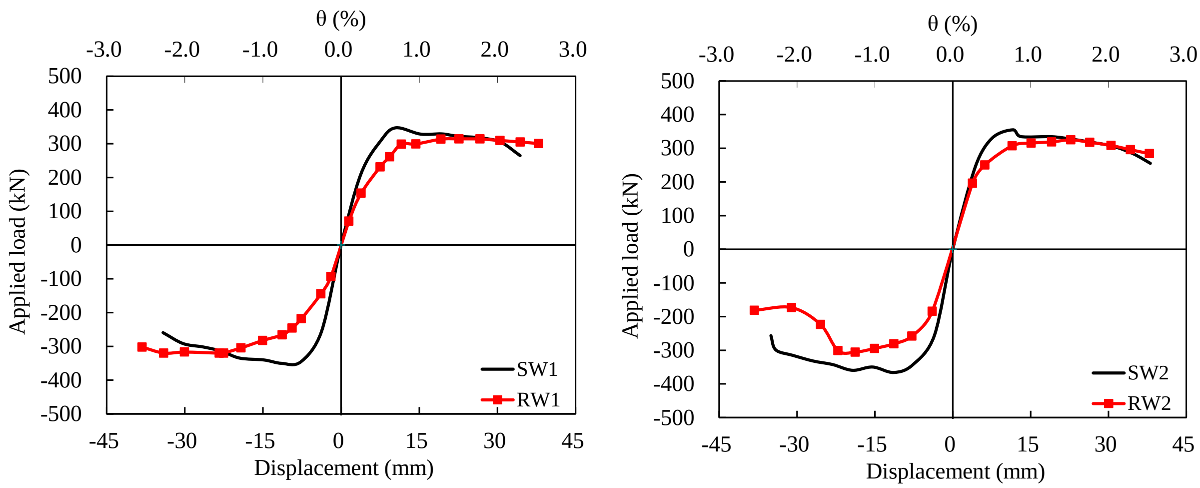

(a) (b)

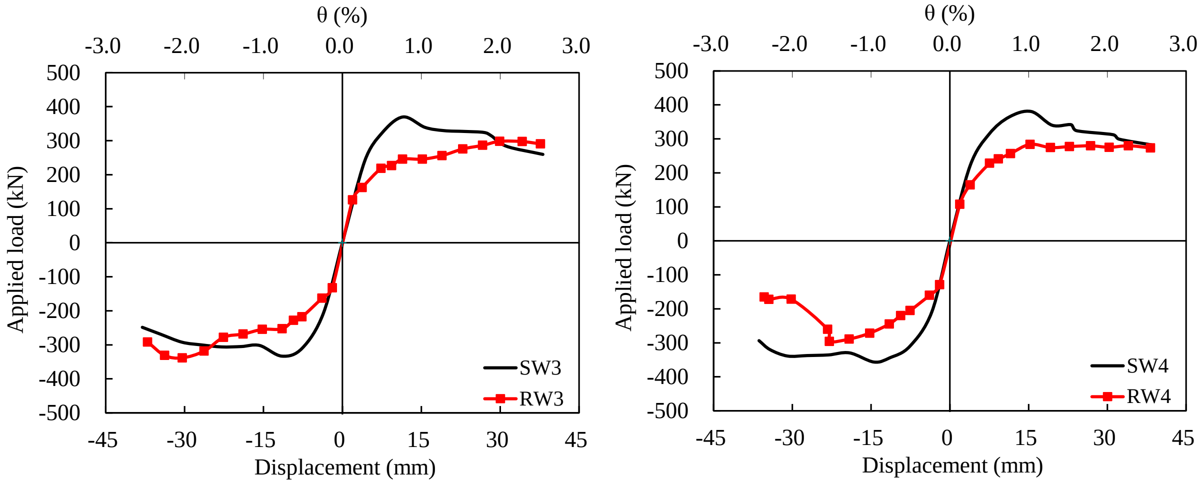

(c) (d)

Fig. 22 Comparison of the envelop of the control and repaired specimens